Biosensors and Bioelectronics 133 (2019) 125–132

Contents lists available at ScienceDirect

Biosensors and Bioelectronics

journal homepage: www.elsevier.com/locate/bios

Porous hollow carbon nanobubbles@ZnCdS multi-shelled dodecahedral cages with enhanced visible-light harvesting for ultrasensitive photoelectrochemical biosensors

Xiong Zhang[a], Jingjun Peng[a], Yibing Song[b], Yaowen Chen[b], Fushen Lu[b], Wenhua Gao[a,b,*]

[a] Department of Chemistry and Laboratory for Preparation and Application of Ordered Structural Materials of Guangdong Province, Shantou University, Shantou, Guangdong 515063, PR China

[b] Analysis & Testing Center, Shantou University, Shantou, Guangdong 515063, PR China

ARTICLE INFO

Keywords:
C@ZnCdS multi-shelled dodecahedral cages
Photoactive material
Photoelectrochemical biosensor
CEA

ABSTRACT

Herein, novel photoactive materials, MOF-derived porous hollow carbon nanobubbles@ZnCdS multi-shelled dodecahedral cages (C@ZnCdS MSDCs) , were synthesized via continuous chemical etching, sulfurization, cation-exchange and calcination strategies. Due to the synergistic effect between the porous shells and the carbon-layer coating , C@ZnCdS MSDCs displayed superior photoelectrochemical (PEC) performance. The synthesized C@ZnCdS MSDCs were assembled onto TiO_2 modified ITO electrodes to form a type-II heterostructures. Then, Au nanoparticles (NPs) were deposited on the surface of ITO/TiO_2/C@ZnCdS MSDCs. Benefiting from the unique structure and performance merits of photoactive materials, a label-free PEC sensing platform based on ITO/TiO_2/C@ZnCdS MSDCs/Au was successfully constructed for CEA detection. Under optimal conditions, the PEC biosensor exhibited a wide linear range (0.00005–500 ng mL^{-1}) and low detection limit (2.28 fg mL^{-1}). The proposed PEC biosensor also showed good stability, specificity, reproducibility and acceptability in human serum. The prepared C@ZnCdS MSDCs would be a promising photoactive material for PEC biosensors. Most importantly, this work opens up new horizons for the application of MOFs-derived hollow carbon materials in sensing.

1. Introduction

Photoelectrochemical (PEC) analysis , as an emerging and promising technology, has gained increasing attention (Ge et al., 2018; Zhao et al., 2015). Thanks to its unparalleled merits of ultra-high sensitivity, low cost, rapid analysis, and easy of miniaturization, PEC biosensors have been used for the detection of various biomolecules, cells, and harmful gases, and so forth (Liu et al., 2018; Wei et al., 2018). Obviously, photoactive materials play a pivotal part in the performance of PEC biosensors. Hitherto, varieties of photoactive materials, such as ZnO (Feng et al., 2018), TiO_2 (Wang et al., 2009), BiOI (Yan et al., 2015), CdS (Han et al., 2018), CdSe (Zhu et al., 2016), and Bi_2S_3 (Yin et al., 2014), have been employed for the construction of photoelectrochemical biosensors. Nevertheless, some inherent defects impede their wide application, such as inefficient visible light absorption, tardigrade charge transfer, high recombination of photoinduced carriers, and so on (Wu et al., 2018). Therefore, the design and synthesis of innovative photoactive materials which have anticipant structure and sensing properties are still urgently needed.

Metal-organic frameworks (MOFs) with unique morphological characteristics have attracted extensive attention in recent years (García-García et al., 2014). Compared with the traditional porous materials, MOFs display some unique merits, including high specific surface area, controllable morphology, high porosity, and easily modification (Ling et al., 2016; Yang et al., 2018). In addition, porous carbon composites derived from MOF can inherit their corresponding structural properties. Moreover, MOF-derived porous carbon structure facilitates electron transport. Thus, they have been widely used in many fields, such as supercapacitors, gas storage, batteries and catalysts (Liu et al., 2016; Shen et al., 2016). It has been reported that MOFs and its derivatives can be used as photoactive materials to construct PEC sensors. For instance, Zhang et al. developed a PEC sensor based on zirconium-porphyrin MOFs for enzyme-free prostate specific antigen detection (Zhang et al., 2018). Lu et al. developed a PEC sensor based

* Corresponding author at: Department of Chemistry and Laboratory for Preparation and Application of Ordered Structural Materials of Guangdong Province, Shantou University, Shantou, Guangdong 515063, PR China.
E-mail address: whgao@stu.edu.cn (W. Gao).

https://doi.org/10.1016/j.bios.2019.03.028
Received 3 January 2019; Received in revised form 1 March 2019; Accepted 15 March 2019
Available online 16 March 2019
0956-5663/

on MOF-derived porous $C_{O3}O_4$ for volatile organic compounds detection (Lu et al., 2014). Zhang et al. developed a PEC sensor based on Zirconium-porphyrin MOFs for label-free phosphoprotein detection (Zhang et al., 2016). Yang et al. developed a PEC sensor based on MOF-derived nitrogen-doped porous carbon-ZnO for label-free alkaline phosphatase detection (Yang et al., 2017). Many efforts have been committed to the application of MOFs and its derivatives to PEC sensing, and considerable progress has been made. However, the application of MOFs and its derivatives as photoactive materials is limited due to poor conductivity, high recombination of photo-induced carrier, and wide bandgap. Therefore, designing a reasonable synthesis strategy based on MOFs to prepare photoactive materials with good electrical conductivity, enhanced charge separation, and narrow bandgap remains a huge challenge.

Inspired by this, herein, MOF-derived porous hollow carbon nanobubbles@ZnCdS multi-shelled dodecahedral cages (C@ZnCdS MSDCs) were prepared by continuous chemical etching, sulfurization, cation-exchange and calcination strategies. To the best of our knowledge, C@ZnCdS MSDCs derived from MOF have not been reported elsewhere, neither has been applied to PEC sensors. The synthesized C@ZnCdS MSDCs exhibit the advantages of hollow nanostructures: (i) hollow nanostructures can facilitate light harvesting due to multiple scattering of light; (ii) the porous thin shells can shorten transport distance of charge, thereby improving the separation efficiency of e^{-1}/h^{+} (Wang et al., 2016; Xiao et al., 2018). It is well known that TiO_2 possesses many advantages, such as high stability, low cost, large surface area, and good photoelectric activity, which are used as an excellent basic material for developing PEC biosensors (Li et al., 2012). However, the intrinsic drawbacks of TiO_2 hinder its widespread application, such as low efficiency of visible light absorption and high recombination of photoinduced e^{-1}/h^{+} pairs (Liu et al., 2017). The synthesized narrow bandgap C@ZnCdS MSDCs (~2.43 eV) were assembled onto TiO_2 modified ITO electrodes to form a type-II heterostructures. The photo-excited electrons were transferred from the conduction band (CB) of C@ZnCdS MSDCs to the CB of TiO_2. Simultaneously, holes were transferred from the valence band (VB) of TiO_2 to the VB of C@ZnCdS MSDCs, leading to boost of visible-light response and separation of photogenerated e^{-1}/h^{+}. Afterward, electrodeposition of Au NPs on ITO/TiO_2/C@ZnCdS MSDCs surface can further ameliorate PEC performance due to its high electron conductivity. Furthermore, the decorated Au NPs can act as an effective electron acceptor for C@ZnCdS MSDCs, suppressing charge recombination. Based on the outstanding PEC performance of ITO/TiO_2/C@ZnCdS MSDCs/Au, a label-free sensing platform was successfully constructed. Here, taking CEA as a model because of its pivotal part in the clinical diagnosis and monitoring of many cancers (Hasanzadeh et al., 2017). The PEC biosensor exhibited a wide linear range (0.00005–500 ng mL^{-1}) with low LOD of 2.28 fg mL^{-1}, indicating that MOF-derived C@ZnCdS MSDCs would be a promising photoactive material for PEC biosensors.

2. Experimental section

Material and reagents, and apparatus have been reported on Supporting information.

2.1. Syntheses of ZIF-8 dodecahedral cages and ZIF-8 yolk-shelled dodecahedral cages

ZIF-8 dodecahedral cages (DCs) were synthesized according to the previous literature with minor modification (Dong et al., 2017). 2.36 g of Zinc nitrate hexahydrate and 1.32 g of 2-methylimidazole were separately dissolved in methanol (100 mL). Then 1.32 g of 2-methylimidazole solution was quickly added into the $Zn(NO_3)_2{\cdot}6H_2O$ solution under stirring. After 1 min, the mixed solution was incubated at room temperature for 11 h. The obtained ZIF-8 DCs were centrifuged, washed with ethanol 3 times, and dried under vacuum at 70 °C for 12 h. ZIF-8 yolk-shelled dodecahedral cages (YSDCs) were prepared by adding 40 mg of as-prepared ZIF-8 DCs to 200 mL of ethanol solution containing 1 g of tannic acid (TA). After stirring 30 min, ZIF-8 YSDCs were collected by centrifugation, washed with ethanol 3 times, and dried under vacuum at 70 °C for 12 h.

2.2. Syntheses of porous hollow ZnS double-shelled dodecahedral cages

20 mg of the as-prepared ZIF-8 YSDCs were placed into 50 mL of ethanol solution containing 400 mg of thioacetamide (TAA). After stirring 3 min, the solution was poured into 100 mL autoclave and heated for 1 h at 150 ℃. Afterward, porous hollow ZnS double-shelled dodecahedral cages (ZnS DSDCs) were collected by centrifugation, washed with ethanol 3 times, and dried under vacuum at 60 °C for 24 h.

2.3. Syntheses of porous hollow nanobubbles ZnCdS double-shelled dodecahedral cages and C@ZnCdS MSDCs

The obtained ZnS DSDCs and 78 mg of $CdCl_2$ were added to 25 mL of ethanol under stirring. Solvothermal cation-exchange reaction was conducted at 160 °C for 4 h. The porous hollow nanobubbles ZnCdS double-shelled dodecahedral cages (ZnCdS DSDCs) were collected by centrifugation, washed with ethanol 3 times, and dried under vacuum at 60 °C for 24 h. Subsequently, the obtained ZnCdS DSDCs were placed in Muffle furnace, and then annealed under air at 450 °C for 30 min with a heating rate of 8.5 °C min^{-1}. Finally, C@ZnCdS MSDCs were obtained.

2.4. Fabrication of ITO/TiO_2/C@ZnCdS MSDCs/Au electrodes

Before modification, the ITO electrodes were successively treated by acetone, 1.0 M NaOH solution, ultrapure water. Firstly, 10 μL of 5.0 mg mL^{-1} TiO_2 aqueous suspension was introduced onto the pre-treated ITO electrode and dried naturally. Subsequently, 6 μL of 5.0 mg mL^{-1} ZnCdS DSDCs aqueous suspension was dropped onto the as-prepared ITO/TiO_2 electrode. After drying, the above electrode was sintered at 450 °C under air for 30 min. The ITO/TiO_2/C@ZnCdS MSDCs electrode was obtained. Afterward, electrodeposition of Au NPs on ITO/TiO_2/C@ZnCdS MSDCs surface was carried out by cyclic voltammetric (CV) scanning from −0.2–0.8 V in 0.5 mM $HAuCl_4$ at a scan rate of 50 mV/s for 10 cycles. After rinsing, the ITO/TiO_2/C@ZnCdS MSDCs/Au electrodes were fabricated successfully. Finally, for comparison, the ITO/TiO_2, ITO/ZnCdS MSDCs, ITO/C@ZnCdS MSDCs, and ITO/TiO_2/C@ZnCdS MSDCs electrodes were prepared in the same manner.

2.5. Construction of the PEC biosensor

Firstly, 8 μL of anti-CEA (30 mg mL^{-1}) was dropped on the above obtained ITO/TiO_2/C@ZnCdS MSDCs/Au electrode surface at 4 °C for 4 h, and then rinsed with PBS. Secondly, the obtained ITO/TiO_2/C@ZnCdS MSDCs/Au/anti-CEA electrode was covered with 6 μL 1 wt% bovine serum albumin in 0.1 M PBS (pH 7.4) for 1 h to block non-specific adsorption, followed by washing with PBS. Finally, 8 μL CEA solutions with different concentrations were dropped onto the electrodes respectively and incubated at 4 °C for 1 h. After rinsing, the PEC biosensor (Scheme 1B) was successfully fabricated and stored at 4 °C until use.

2.6. PEC measurements

The PEC measurements were performed using a photoelectrochemical workstation in 0.1 M PBS (pH 7.4) solution containing 0.2 M ascorbic acid (AA). The applied potential was 0 V with a 430 nm light as excitation source and a light intensity of 180 W m^{-2}. A three-electrode system was used with a saturated Ag/AgCl electrode as the

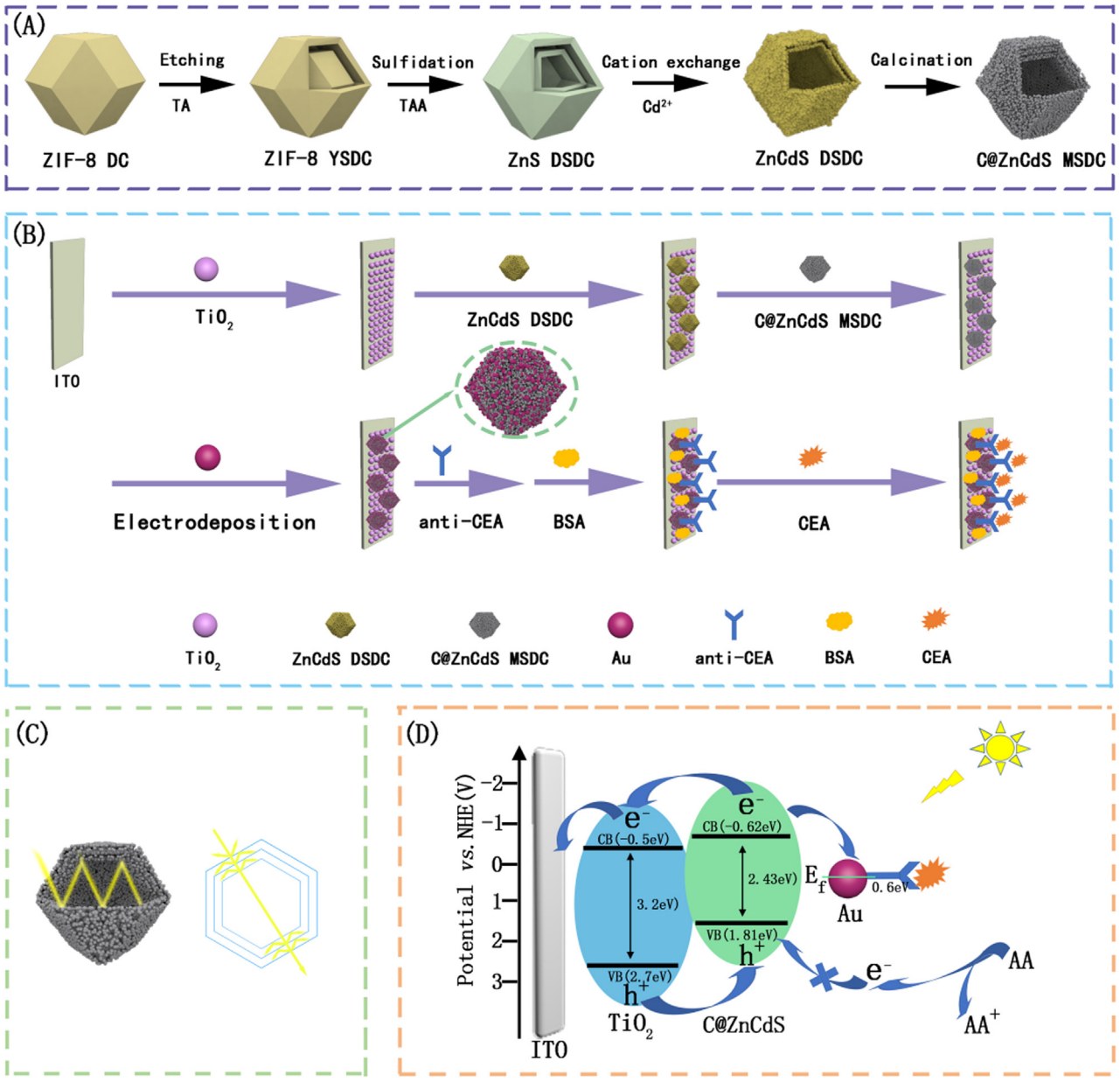

Scheme 1. (A) Schematic illustration of the synthesis process of C@ZnCdS MSDCs. (B) Construction process of PEC biosensor for CEA detection. (C) Schematic illustration of the light harvesting of C@ZnCdS MSDCs. (D) Photogenerated electron-hole transfer mechanism based on TiO_2/C@ZnCdS MSDCs/Au.

reference electrode, a Pt wire as the counter electrode, and the as-prepared TiO_2/C@ZnCdS MSDCs/Au modified ITO electrode ($3.0 \times 1.0\ cm^2$) as the working electrode.

3. Results and discussion

3.1. Characterization of C@ZnCdS MSDCs

The synthesis procedure of C@ZnCdS MSDCs is schematically depicted in Scheme 1A. First, ZIF-8 DCs are synthesized by self-assembly of Zn^{2+} ions and 2-methylimmidazole. The obtained ZIF-8 DCs are then converted to ZIF-8 YSDCs by a polymer acid etching. In this process, TA which acts as etchant and protector releases protons to penetrate the surface and reach the central region of the ZIF-8 DCs (Zhang et al., 2017b). Simultaneously, it is uniformly adsorbed on the surfaces of the ZIF-8 DCs due to planar conformation and abundance of hydroxyl group, thus protecting the outer region of the ZIF-8 DCs (Hu et al., 2016; Zhang et al., 2017a). Subsequently, Zn^{2+} ions located on the surface of the ZIF-8 DCs react with S^{2-} ions released from TAA in the solvothermal treatment, ultimately, forming ZnS DSDCs. To prepare the C@ZnCdS MSDCs, a metal cation-exchange reaction between Zn^{2+} and Cd^{2+} is performed. Since the solubility product constant (K_{sp}) of ZnS (1.6×10^{-24}) is larger than CdS (8.0×10^{-27}), the structural conversion of ZnS DSDCs to ZnCdS DSDCs is induced by ion exchange (Chen et al., 2017; Choi et al., 2016). Afterwards, the C@ZnCdS MSDCs are fabricated by the carbonization of ZnCdS DSDCs.

The microstructure and morphology of as-prepared samples are obtained by FESEM analysis, as shown in Fig. 1. The ZIF-8 DCs (Fig. 1A) and ZIF-8 YSDCs (Fig. 1B) exhibit a typical rhombic dodecahedron with an average particle size of about 800 nm. Besides, the ZIF-8 YSDCs have the same crystal structure as ZIF-8 DCs (Fig. S1). It is noteworthy that the ZnS DSDCs (Fig. 1C) have a unique double-shelled structure. Then, the obtained ZnS DSDCs are converted into double-shelled ZnCdS DCs (Fig. 1D) through a solvothermal cation-exchange reaction at 160 °C. The triple-shelled C@ZnCdS DCs are obtained after calcining the double-shelled ZnCdS DCs precursor in Muffle furnace, with similar

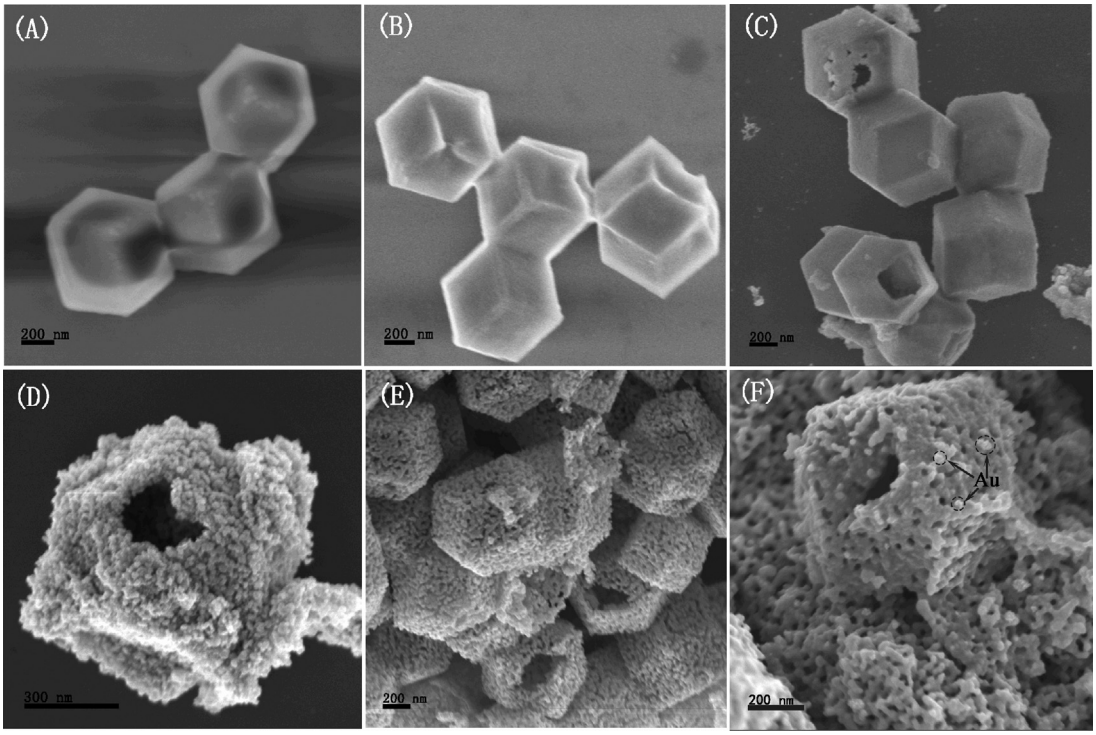

Fig. 1. FESEM images of (A) ZIF-8 DCs. (B) ZIF-8 YSDCs. (C) ZnS DSDCs. (D) ZnCdS DSDCs. (E) C@ZnCdS MSDCs. (F) TiO_2/C@ZnCdS MSDCs/Au composites.

rhombic dodecahedron structure and size being maintained. Besides, the obtained C@ZnCdS MSDCs have a pore diameter distribution in the range of 25–40 nm (Fig. 1E).

TEM image (Fig. 2A, B) clearly exhibits the unique triple-shelled hollow structure. The microstructure of C@ZnCdS MSDCs is further elucidated by high-resolution TEM (HRTEM) lattice image (Fig. 2C) and selected area electron diffraction (SAED) pattern (Fig. 2D). The marked lattice spacing of 0.33 nm and 0.19 nm corresponds to that of (002) and (110) plane of CdS (JCPDS, No. 77-2306) and ZnS (JCPDS, No. 75-1547), respectively. The SAED pattern (Fig. 2D) obtained from a single cage exhibits bright diffraction rings, indicating the cage is polycrystalline (Jiang et al., 2012). In addition, high-angle annular dark-field scanning transmission electron microscopy (HAADF-STEM) further reveals a carbon-layer coating on the surface of material (Fig. 2E). Elemental mapping images indicate the uniform distribution of Zn, Cd, S and C elements in C@ZnCdS MSDCs. Thus, through the sequential chemical etching, sulfurization and calcination strategy, porous hollow carbon nanobubbles@ZnCdS triple-shelled dodecahedral cages are obtained.

PXRD pattern is utilized to further investigate the crystal structure of C@ZnCdS MSDCs. In Fig. 3A, the characteristic peaks at 24.8°, 26.5°, 28.2°, 36.7°, 43.7°,47.9°, and 51.9°observed in PXRD patterns match well with the standard CdS (JCPDS, No. 77–2306), the peaks at 26.8°, 28.4°, 47.4°, and 51.6° can be assigned to ZnS (JCPDS, No. 75-1547).

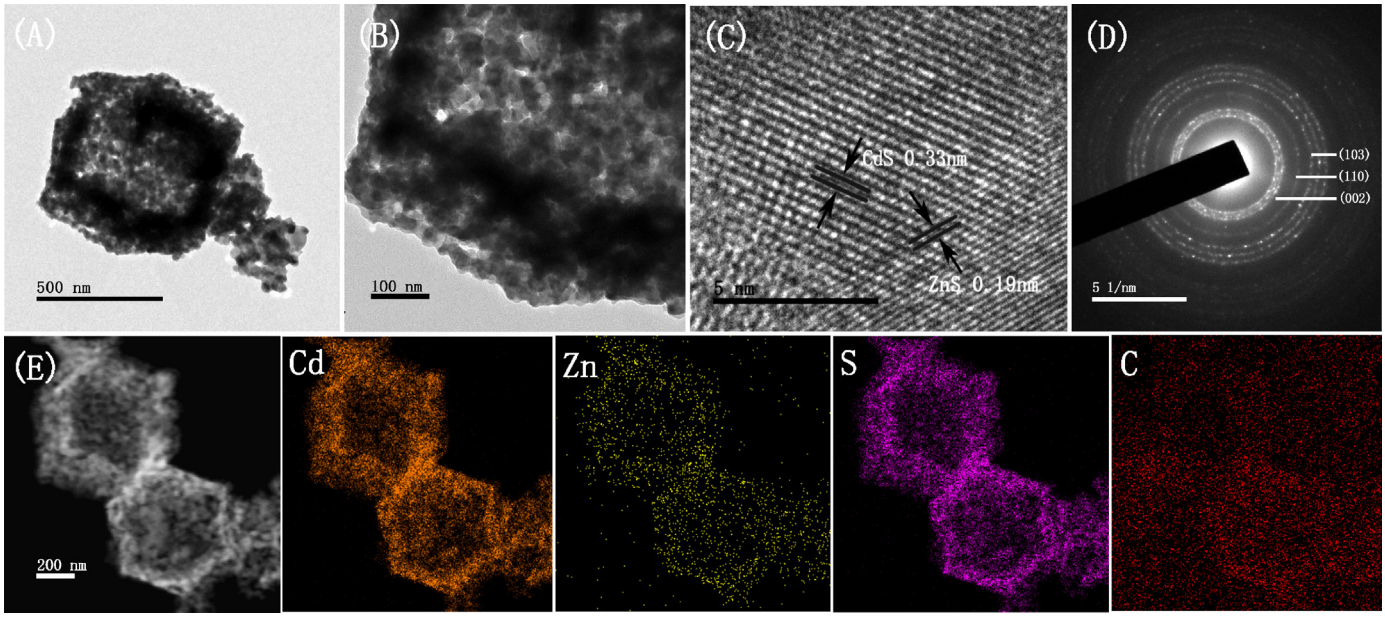

Fig. 2. C@ZnCdS MSDCs. (A, B) TEM. (C, D) HRTEM lattice image and SAED. (E) HAADF-STEM and elemental mapping images of Cd, Zn, S, C elementals.

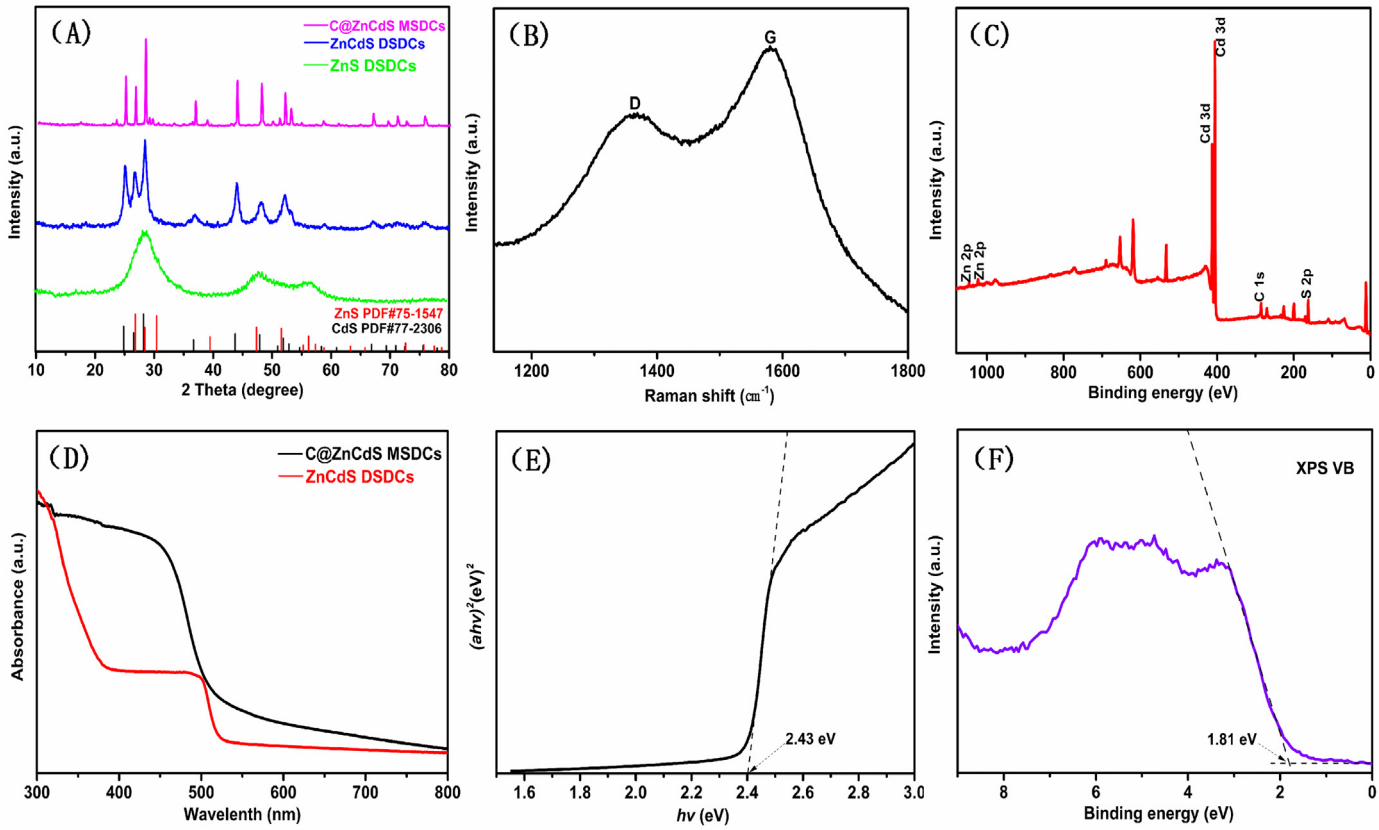

Fig. 3. (A) XRD pattern. (B) Raman spectra of C@ZnCdS MSDCs. (C) XPS spectrum of C@ZnCdS MSDCs. (D) UV-Vis diffuse reflectance spectra. (E) Plots of $(ahv)^2$ vs photon energy (hv) for C@ZnCdS MSDCs. (F) VB XPS of C@ZnCdS MSDCs.

The Raman spectra of C@ZnCdS MSDCs are displayed in Fig. 3B. The typical D-band and G-band are observed at approximately 1350 cm^{-1} and 1585 cm^{-1}, respectively, and the intensity of the G-band is greatly enhanced compared to the D-band, indicating a significant increase in the degree of graphitization (Chen et al., 2013; Niu et al., 2017).

The elemental composition and chemical bonding state of C@ZnCdS MSDCs are further analyzed using XPS. As shown in Fig. 3C, Zn, Cd, S, C can be confirmed in the XPS survey spectra of the sample. Primarily, the high-resolution XPS spectrum of Zn 2p is shown in Fig. S2. The two prominent bands at 1022.4 and 1045.8 eV correspond to Zn $2p_{3/2}$ and Zn $2p_{1/2}$ peaks of Zn^{2+} (Fig. S2A), respectively (Jing et al., 2017; Yang et al., 2014). The Cd 3d spectrum (Fig. S2B) shows two distinct bands at 412.1 and 405.3 eV, which are easily assigned to the Cd $3d_{3/2}$ and Cd $3d_{5/2}$ peaks of Cd^{2+}, respectively. Besides, the S 2p spectrum (Fig. S2C) confirms the chemical bonding state of S^{2-} at 161.6 and 162.9 eV in the S-Cd/S-Zn bonded structure. Additionally, it is noted that the C 1s peak (Fig. S2D) at 284.7 eV correspond to C-S (Zhou et al., 2015).

The UV-visible DRS is conducted to further evaluate the optical properties of C@ZnCdS MSDCs and ZnCdS DSDCs (Fig. 3D). Compared to ZnCdS DSDCs, C@ZnCdS MSDCs exhibits significantly increased visible-light absorption intensity and a broaden absorption range. The distinct differences in optical properties are primarily ascribed to the following two points: (i) the obtained C@ZnCdS MSDCs with triple porous thin shells can sufficiently absorb incident light through the reflection effect between shells; (ii) the introduction of the carbon shell improves electrical conductivity and facilitates electron transport. The results indicate that C@ZnCdS MSDCs should be suitable photoactive materials to construct PEC biosensors.

3.2. Characterization of TiO_2/C@ZnCdS MSDCs/Au composites

The microstructure and morphology of TiO_2/C@ZnCdS MSDCs/Au composites are characterized by FESEM (Fig. 1F). Additionally, the PXRD analyses of TiO_2, C@ZnCdS MSDCs, and TiO_2/C@ZnCdS MSDCs/Au composites are shown in Fig. 4A. The other details are provided in Supporting information.

3.3. PEC mechanism

The photo-generated e^{-1}/h^{+} transfer mechanism of TiO_2/C@ZnCdS MSDCs/Au for the PEC biosensor is showed in Scheme 1D. The bandgap energy (Eg) of the as-synthesized ZnCdS DSDCs and C@ZnCdS MSDCs could be estimated using the empirical equation:

$$ahv = A(hv - Eg)^{1/2} \quad (1)$$

where a, A, and hv are the absorption coefficient, a constant, the photon energy, respectively (Kaur and Nagaraja, 2017).

The Eg values of ZnCdS DSDCs (Fig. S4) and C@ZnCdS MSDCs (Fig. 3E) were calculated (Eq. (1)) to be 2.46 and 2.43 eV, respectively. This result suggests that triple-shelled porous carbon nanoarchitecture can significantly enhance visible-light harvesting and accelerate electron transfer. The VB potentials of C@ZnCdS MSDCs were measured by VB-XPS (Fig. 3F), with band edges of 1.81 eV. The CB potentials of C@ZnCdS MSDCs can be calculated by the following empirical formulae (Song et al., 2016):

$$E_{CB} = E_{VB} - E_g \quad (2)$$

where E_{CB} and E_{VB} are the CB and VB edge potentials, respectively.

The E_{CB} potentials of C@ZnCdS MSDCs was calculated (Eq. (2)) to be $E_{CB} = -0.62$ eV. The E_{CB} potentials and E_{VB} potentials of TiO_2 were −0.5 (NHE) and 2.7 (NHE) eV (Li et al., 2013, 2011). As shown in Scheme 1D, C@ZnCdS MSDCs and TiO_2 have interlaced band structures, in which both CB and VB positions of C@ZnCdS MSDCs are higher than TiO_2. Therefore, the synthesized narrow bandgap

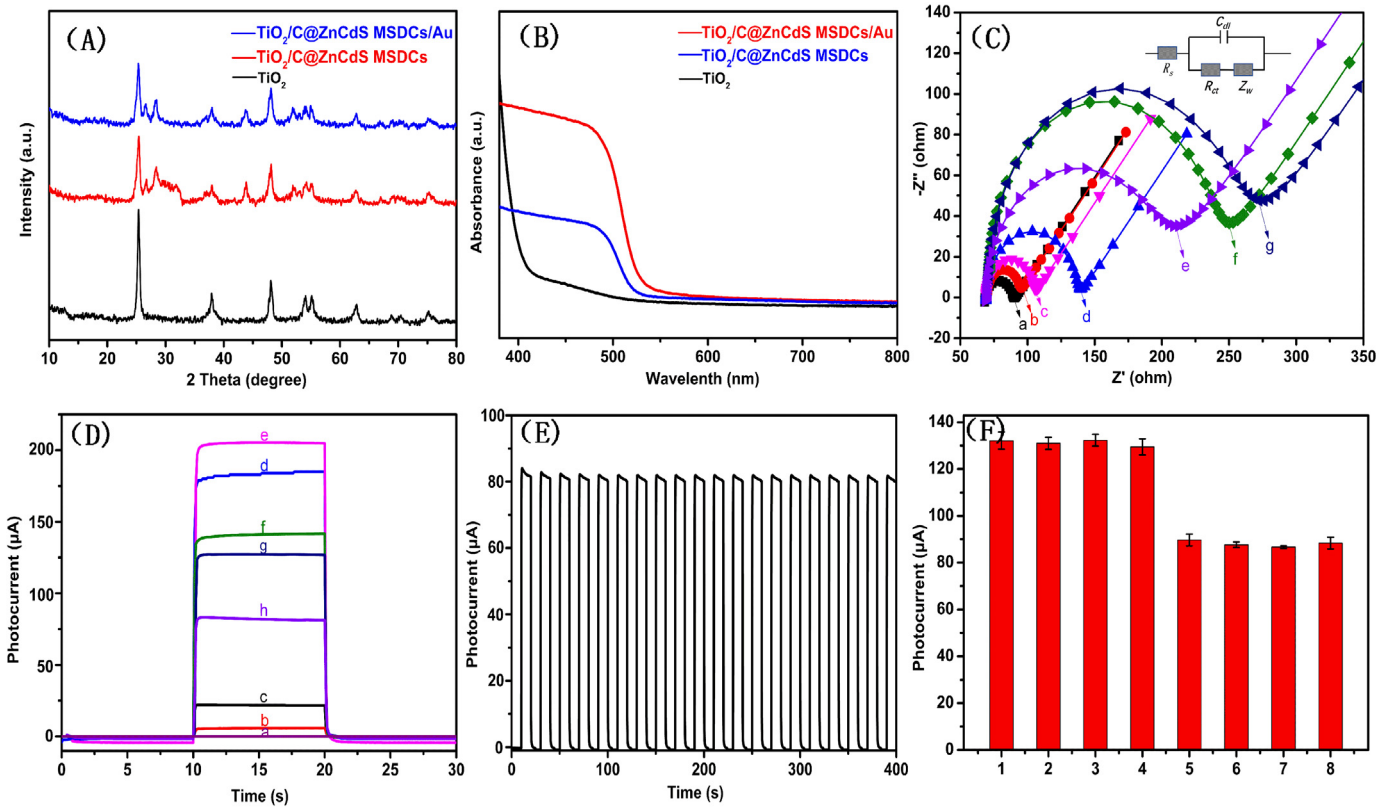

Fig. 4. (A) XRD pattern. (B) UV-Visible diffuse reflectance spectra. (C) EIS Nyquist plots of bare ITO (a), ITO/TiO_2 (b), ITO/TiO_2/C@ZnCdS MSDCs/Au (c), ITO/TiO_2/C@ZnCdS MSDCs (d), ITO/TiO_2/C@ZnCdS MSDCs/Au/anti-CEA (e), ITO/TiO_2/C@ZnCdS MSDCs/Au/anti-CEA/BSA (f), ITO/TiO_2/C@ZnCdS MSDCs/Au/anti-CEA/BSA/CEA (g). (D) Time-based photocurrent response curves of (a) bare ITO, (b) ITO/TiO_2, (c) after calcinations ITO/TiO_2, (d) ITO/TiO_2/C@ZnCdS MSDCs, (e) ITO/TiO_2/C@ZnCdS MSDCs/Au, (f) ITO/TiO_2/C@ZnCdS MSDCs/Au/anti-CEA, (g) ITO/TiO_2/C@ZnCdS MSDCs/Au/anti-CEA/BSA, (h) ITO/TiO_2/C@ZnCdS MSDCs/Au/anti-CEA/BSA/CEA. (E) Photocurrent response of the PEC biosensor under several on/off irradiation cycles for 400 s, C_{CEA} = 0.1 ng mL^{-1}. (F) Selectivity of the PEC biosensors to CEA, (1) blank, (2) blank + 100 ng mL^{-1} BSA, (3) blank + 100 ng mL^{-1} AFP, (4) blank + 100 ng mL^{-1} PSA, (5) 0.1 ng mL^{-1} CEA, (6) 0.1 ng mL^{-1} CEA + 100 ng mL^{-1} BSA, (7) 0.1 ng mL^{-1} CEA + 100 ng mL^{-1} AFP, (8) 0.1 ng mL^{-1} CEA + 100 ng mL^{-1} PSA. EIS experiments were conducted in 0.1 mM KCl solution containing 5 mM $[Fe(CN)6]^{3-/4-}$ at frequencies ranging from 0.1 Hz to 100 kHz with a signal amplitude of 5 mV.

(~2.43 eV) C@ZnCdS MSDCs were assembled onto TiO_2 modified ITO electrodes to form a type-II heterostructures. The photoexcited electrons were transferred from the CB of C@ZnCdS MSDCs to the CB of TiO_2. Simultaneously, holes were transferred from the VB of TiO_2 to the VB of C@ZnCdS MSDCs and then scavenged by an electron donor AA, resulting in enhanced visible-light response and efficient separation of photo-generated e^{-1}/h^{+} (Li et al., 2015). In addition, because the Fermi level of Au (+0.6 V vs. NHE) (Misra et al., 2014) is lower than the conduction band edge of C@ZnCdS MSDCs (-0.62 V vs. NHE), the decorated Au can act as an effective electron acceptor for C@ZnCdS MSDCs, prohibiting charge recombination (Chiu et al., 2018). Thus, the photocurrent response of the biosensor is enhanced significantly. When anti-CEA and CEA are specifically bound, the electron transfer from AA to TiO_2/C@ZnCdS MSDCs/Au composites is hindered, resulting in a decreased photocurrent.

The UV-visible DRS is conducted to further evaluate the optical properties of TiO_2/C@ZnCdS MSDCs/Au. In Fig. 4B, the absorption wavelength of TiO_2 is apparently lower than 400 nm attributed to the wide bandgap (3.2 eV), leading to low efficiency of visible light absorption (Wang et al., 2017). However, TiO_2/C@ZnCdS MSDCs composite is extended into the visible light region up to ~550 nm due to the unique morphological features of C@ZnCdS MSDCs and the formation of the type-II heterostructure. On the one hand, the synthesized C@ZnCdS MSDCs exhibit unique morphological advantages of hollow nanostructures (Scheme 1C): (i) the superior light-capturing capability can be mainly ascribed to multiple scattering and reflection in multi-shell porous hollow nanobubble structure (Qian et al., 2009); (ii) triple-shell structure can shorten the transport distance of charge, hence suppressing the charge recombination (Xiao et al., 2018); (iii) the introduction of the carbon shell facilitates electron transport. On the other hand, the type-II TiO_2/C@ZnCdS MSDCs heterostructures can significantly enhance the visible-light response and suppresses the recombination of photogenerated e^{-}/h^{+}. Particularly, the electrodeposition of Au NPs on ITO/TiO_2/C@ZnCdS MSDCs shows a broader absorption range and apparently enhanced visible-light absorption intensity, which is attributed to Au NPs as an effective electron acceptor for C@ZnCdS MSDCs, suppressing charge recombination.

3.4. PEC behaviors and EIS

EIS is an effective tool for characterizing interface properties of the electrodes, which can be used to further study the stepwise assembly process of the biosensor (Fig. 4C) (Ge et al., 2017). The electron-transfer resistance (R_{et}) value of the bare ITO electrode exhibited the smallest (curve a), which could be attributed to the fast electrons transfer of the sensing interface. Afterwards, the R_{et} constantly increased when TiO_2 (curves b), C@ZnCdS MSDCs (curves d) were assembled on the bare ITO surface, which could be attributed to the poor electron transmission capacity of different substances. Nevertheless, after electrodeposition Au NPs on ITO/TiO_2/C@ZnCdS MSDCs surface (curves c), a smaller R_{et} was obtained by increased conductivity. After continuous modification with anti-CEA (curve e), BSA (curve f) and CEA (curve g), the R_{et} value increased progressively, which could be due to the hindrance effect and poor conductivity of protein. The results

indicate that PEC biosensor was prepared successfully.

To deeply analyze the stepwise construction process of the PEC biosensor, all PEC tests was carried out in PBS (0.1 M, pH 7.4) solution containing 0.2 M AA (Fig. 4D). No photocurrent was observed on the bare ITO electrode (curve a). After modified with TiO_2, the photocurrent intensity (curve b, I = 6.58 μA) of ITO/TiO_2 electrode increased slightly. However, the ITO/TiO_2 electrode annealed at 450° for 30 min in air displayed enhancive photocurrent intensity (curve c, I = 22.48 μA) which was ascribed to the porous structure of calcined TiO_2 (Fig. S3A). The photocurrent intensity (curve d, I = 190.23 μA) of ITO/TiO_2/C@ZnCdS MSDCs electrode displayed a ~8.5 times higher than that of ITO/TiO_2 electrode (curve c), ascribed to the truth that complex triple-shelled hollow structures could promote light absorption properties. After electrodeposition Au NPs on ITO/TiO_2/C@ZnCdS MSDCs electrode surface, the photocurrent intensity (curve e, I = 206.88 μA) of ITO/TiO_2/C@ZnCdS MSDCs/Au electrode was increased slightly owing to the enlarged electron-hole separation. When anti-CEA (curve f, I = 143.24 μA), BSA (curve g, I = 129.86 μA) and CEA (curve h, I = 84.58 μA) were incubated on ITO/TiO_2/C@ZnCdS MSDCs/Au electrode surface successively, the photocurrents decrease gradually, owing to the hindrance effect and poor conductivity of protein.

3.5. Stability, reproducibility, and selectivity of the PEC biosensor

The stability of the fabricated PEC biosensor is shown in Fig. 4E. The photocurrent response of the biosensor was recorded under ten on/off irradiation cycles for 400 s with 0.1 ng mL^{-1} CEA and no significant variation was observed, suggesting the PEC biosensor possesses stable photocurrent response for CEA detection. In addition, the reproductivity of the PEC biosensor was also investigated. For 0.1 ng mL^{-1} CEA, the relative standard deviation (RSD) of 2.5% (92.24 μA, 88.23 μA, 89.63 μA, 87.84 μA, 92.68 μA) was obtained for five ITO/TiO_2/C@ZnCdS MSDCs/Au/anti-CEA/BSA/CEA electrodes, indicating the designed biosensor has excellent reproducibility. Furthermore, the selectivity of the PEC biosensor for CEA was studied by testing the photocurrent response of the sensor to several representative interfering substances including prostate specific antigen (PSA), alpha-fetoprotein (AFP), and BSA. No dramatic photocurrent signals change was observed by interfering substances, suggesting that the proposed PEC sensor has satisfactory selectivity (Fig. 4F).

3.6. PEC assay of CEA

To achieve excellent performance in the PEC detection of CEA, experimental parameters including pH values, immunoreaction time, incubation time, the concentration of C@ZnCdS MSDCs, AA and anti-CEA were optimized (Fig. S5). Fig. 5A shows that the fabricated PEC biosensor is applied to detect different concentrations of CEA under optimized conditions. The photocurrent response gradually decreases with increasing concentrations of CEA. Fig. 5B displays the linear relationship related to the logarithmic values of CEA concentration from 0.00005 ng mL^{-1} to 500 ng mL^{-1} with low LOD of 2.28 fg mL^{-1} (S/N = 3). The regression equation is I (μA) = 78.7823–9.4528 log C_{CEA} (ng mL^{-1}) (R^2 = 0.9981). The fabricated PEC biosensor for CEA assay showed a relatively wider linear range and lower detection limits than that recently reported (Table S1).

3.7. Application of the biosensor in human serum

To assess the practical applications of the proposed PEC biosensor, different concentrations (0.10, 10.00, 100.00 ng mL^{-1}) of CEA in human serum samples were detected by standard addition methods. As shown in Table S2, the RSD was 1.73–3.79% and recoveries were 97.3–105.7%, indicating the practicability of designed PEC biosensor for CEA detection in serum samples.

4. Conclusion

In summary, C@ZnCdS MSDCs with triple porous thin shells were successfully synthesized for the first time and used as a photoactive material for PEC biosensor. Benefiting from its unique morphological characteristics, C@ZnCdS MSDCs exhibited significantly enhanced visible-light harvesting. The construction of TiO_2/C@ZnCdS MSDCs heterostructure can effectively suppresses the recombination of photogenerated e^{-1}/h^{+}. Moreover, after Au NPs deposited on the surface of ITO/TiO_2/C@ZnCdS MSDCs, the absorption capacity of visible light was further enhanced. Meanwhile, the PEC mechanism of TiO_2/C@ZnCdS MSDCs/Au system was initially studied. The proposed PEC biosensor exhibited a low detection limit and wide linear range, excellent selectivity, stability, and reproducibility in CEA analysis.

In this paper, the application of C@ZnCdS MSDCs as photoactive material in PEC biosensor was initially explored. Further work will center on the optimization of experimental conditions and the construction of novel heterojunctions.

Acknowledgements

We are grateful for the financial support from the Natural Science Foundation of Guangdong Province (No. 2014A030313480), the Science & Technology Project of Guangdong Province (No. 2013B030600001 & No. 2016A020223014).

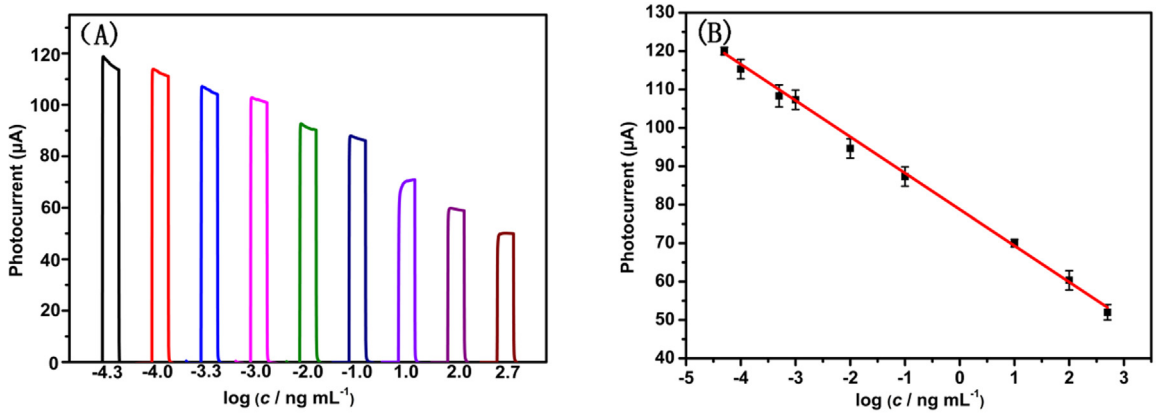

Fig. 5. (A) Photocurrent responses of the PEC biosensor in the presence of 0.00005, 0.0001, 0.0005, 0.001, 0.01, 0.1, 10, 100, and 500 ng mL^{-1} CEA (from left to right). (B) The corresponding logarithmic calibration curve for CEA detection.

Appendix A. Supporting information

Supplementary data associated with this article can be found in the online version at doi:10.1016/j.bios.2019.03.028.

References

Chen, J., Chen, J., Li, Y., 2017. J. Mater. Chem. A 5, 24116–24125.
Chen, Y., Li, X., Park, K., Song, J., Hong, J., Zhou, L., Mai, Y.W., Huang, H., Goodenough, J.B., 2013. J. Am. Chem. Soc. 135, 16280–16283.
Chiu, Y.-H., Chang, K.-D., Hsu, Y.-J., 2018. J. Mater. Chem. A 6, 4286–4296.
Choi, W., Park, G., Bae, K.-L., Choi, J.Y., Nam, K.M., Song, H., 2016. J. Mater. Chem. A 4, 13414–13418.
Dong, S., Li, C., Ge, X., Li, Z., Miao, X., Yin, L., 2017. ACS Nano 11, 6474–6482.
Feng, J., Li, F., Li, X., Wang, Y., Fan, D., Du, B., Li, Y., Wei, Q., 2018. Biosens. Bioelectron. 117, 773–780.
García-García, P., Müller, M., Corma, A., 2014. Chem. Sci. 5, 2979.
Ge, L., Li, H., Du, X., Zhu, M., Chen, W., Shi, T., Hao, N., Liu, Q., Wang, K., 2018. Biosens. Bioelectron. 111, 131–137.
Ge, S., Lan, F., Liang, L., Ren, N., Li, L., Liu, H., Yan, M., Yu, J., 2017. ACS Appl. Mater. Interfaces 9, 6670–6678.
Han, Q., Wang, R., Xing, B., Chi, H., Wu, D., Wei, Q., 2018. Biosens. Bioelectron. 106, 7–13.
Hasanzadeh, M., Shadjou, N., Lin, Y., de la Guardia, M., 2017. Trends Anal. Chem. 86, 185–205.
Hu, M., Ju, Y., Liang, K., Suma, T., Cui, J., Caruso, F., 2016. Adv. Funct. Mater. 26, 5827–5834.
Jiang, Z., Sun, H., Qin, Z., Jiao, X., Chen, D., 2012. Chem. Commun. 48, 3620–3622.
Jing, M., Chen, Z., Li, Z., Li, F., Chen, M., Zhou, M., He, B., Chen, L., Hou, Z., Chen, X., 2017. ACS Appl. Mater. Interfaces 10, 704–712.
Kaur, M., Nagaraja, C.M., 2017. ACS Sustain. Chem. Eng. 5, 4293–4303.
Li, H., Zhou, Y., Tu, W., Ye, J., Zou, Z., 2015. Adv. Funct. Mater. 25, 998–1013.
Li, K., Chai, B., Peng, T., Mao, J., Zan, L., 2013. ACS Catal. 3, 170–177.
Li, W., Li, D., Meng, S., Chen, W., Fu, X., Shao, Y., 2011. Environ. Sci. Technol. 45, 2987–2993.
Li, Y.J., Ma, M.J., Zhu, J.J., 2012. Anal. Chem. 84, 10492–10499.
Ling, P., Lei, J., Ju, H., 2016. Anal. Chem. 88, 10680–10686.
Liu, P.P., Liu, X., Huo, X.H., Tang, Y., Xu, J., Ju, H., 2017. ACS Appl. Mater. Interfaces 9, 27185–27192.
Liu, S., He, P., Hussain, S., Lu, H., Zhou, X., Lv, F., Liu, L., Dai, Z., Wang, S., 2018. ACS Appl. Mater. Interfaces 10, 6618–6623.
Liu, T.-Z., Hu, R., Zhang, X., Zhang, K.-L., Liu, Y., Zhang, X.-B., Bai, R.-Y., Li, D., Yang, Y.-H., 2016. Anal. Chem. 88, 12516–12523.
Lu, Y., Zhan, W., He, Y., Wang, Y., Kong, X., Kuang, Q., Xie, Z., Zheng, L., 2014. ACS Appl. Mater. Interfaces 6, 4186–4195.
Misra, M., Kapur, P., Nayak, M.K., Singla, M., 2014. New J. Chem. 38, 4197–4203.
Niu, J.L., Zeng, C.H., Peng, H.J., Lin, X.M., Sathishkumar, P., Cai, Y.P., 2017. Small 13, 1702150.
Qian, J., Liu, P., Xiao, Y., Jiang, Y., Cao, Y., Ai, X., Yang, H., 2009. Adv. Mater. 21, 3663–3667.
Shen, K., Chen, X., Chen, J., Li, Y., 2016. ACS Catal. 6, 5887–5903.
Song, C., Feng, Y., Shi, W., Liu, C., 2016. CrystEngComm 18, 7796–7804.
Wang, G.L., Xu, J.J., Chen, H.Y., Fu, S.Z., 2009. Biosens. Bioelectron. 25, 791–796.
Wang, X., Feng, J., Bai, Y., Zhang, Q., Yin, Y., 2016. Chem. Rev. 116, 10983–11060.
Wang, Y., Ge, S., Zhang, L., Yu, J., Yan, M., Huang, J., 2017. Biosens. Bioelectron. 89, 859–865.
Wei, J., Chang, W., Qileng, A., Liu, W., Zhang, Y., Rong, S., Lei, H., Liu, Y., 2018. Anal. Chem. 90, 9606–9613.
Wu, T., Yan, T., Zhang, X., Feng, Y., Wei, D., Sun, M., Du, B., Wei, Q., 2018. Biosens. Bioelectron. 117, 575–582.
Xiao, M., Wang, Z., Lyu, M., Luo, B., Wang, S., Liu, G., Cheng, H.M., Wang, L., 2018. Adv. Mater. 1801369.
Yan, K., Liu, Y., Yang, Y., Zhang, J., 2015. Anal. Chem. 87, 12215–12220.
Yang, L., Zeng, X., Wang, W., Cao, D., 2018. Adv. Funct. Mater. 28, 1704537.
Yang, R., Yan, X., Li, Y., Zhang, X., Chen, J., 2017. ACS Appl. Mater. Interfaces 9, 42482–42491.
Yang, X., Xue, H., Xu, J., Huang, X., Zhang, J., Tang, Y.B., Ng, T.W., Kwong, H.L., Meng, X.M., Lee, C.S., 2014. ACS Appl. Mater. Interfaces 6, 9078–9084.
Yin, H., Sun, B., Zhou, Y., Wang, M., Xu, Z., Fu, Z., Ai, S., 2014. Biosens. Bioelectron. 51, 103–108.
Zhang, G., Shan, D., Dong, H., Cosnier, S., Al-Ghanim, K.A., Ahmad, Z., Mahboob, S., Zhang, X., 2018. Anal. Chem. 90, 12284–12291.
Zhang, G.Y., Zhuang, Y.H., Shan, D., Su, G.F., Cosnier, S., Zhang, X.J., 2016. Anal. Chem. 88, 11207–11212.
Zhang, P., Guan, B.Y., Yu, L., Lou, X.W.D., 2017a. Angew. Chem., Int. Ed. 56, 7141–7145.
Zhang, W., Jiang, X., Zhao, Y., Carne-Sanchez, A., Malgras, V., Kim, J., Kim, J.H., Wang, S., Liu, J., Jiang, J.S., Yamauchi, Y., Hu, M., 2017b. Chem. Sci. 8, 3538–3546.
Zhao, W.W., Xu, J.J., Chen, H.Y., 2015. Chem. Soc. Rev. 44, 729–741.
Zhou, J., Lian, J., Hou, L., Zhang, J., Gou, H., Xia, M., Zhao, Y., Strobel, T.A., Tao, L., Gao, F., 2015. Nat. Commun. 6, 8503.
Zhu, H., Fan, G.C., Abdel-Halim, E.S., Zhang, J.R., Zhu, J.J., 2016. Biosens. Bioelectron. 77, 339–346.